

## ARTICLE OPEN



# Low-frequency spin qubit energy splitting noise in highly purified $^{28}\text{Si}/\text{SiGe}$

Tom Struck<sup>1</sup>, Arne Hollmann<sup>1</sup>, Floyd Schauer<sup>2</sup>, Olexiy Fedorets<sup>1</sup>, Andreas Schmidbauer<sup>2</sup>, Kentarou Sawano<sup>3</sup>, Helge Riemann<sup>4</sup>, Nikolay V. Abrosimov<sup>4</sup>, Łukasz Cywiński<sup>5</sup>, Dominique Bougeard<sup>2</sup> and Lars R. Schreiber<sup>1</sup>

We identify the dominant source for low-frequency spin qubit splitting noise in a highly isotopically-purified silicon device with an embedded nanomagnet and a spin echo decay time  $T_2^{\text{echo}} = 128 \mu\text{s}$ . The power spectral density (PSD) of the charge noise explains both, the clear transition from a  $1/f^2$ - to a  $1/f$ -dependence of the splitting noise PSD as well as the experimental observation of a decreasing time-ensemble spin dephasing time, from  $T_2^* \approx 20 \mu\text{s}$ , with increasing measurement time over several hours. Despite their strong hyperfine contact interaction, the few  $^{73}\text{Ge}$  nuclei overlapping with the quantum dot in the barrier do not limit  $T_2^*$ , likely because their dynamics is frozen on a few hours measurement scale. We conclude that charge noise and the design of the gradient magnetic field are the key to further improve the qubit fidelity in isotopically purified  $^{28}\text{Si}/\text{SiGe}$ .

npj Quantum Information (2020)6:40; <https://doi.org/10.1038/s41534-020-0276-2>

## INTRODUCTION

Gate-defined quantum dots (QDs) are a promising platform to confine and control single spins, which can be exploited as quantum bits (qubits)<sup>1</sup>. Unlike charge, a single spin does not couple directly to electric noise. Dephasing is dominated by magnetic noise, typically from the nuclear spin bath overlapping with the QD<sup>2</sup>. The use of silicon as a qubit host material boosted the control of individual spins by minimizing this magnetic noise: in addition to the intrinsically low hyperfine interaction in natural silicon, the existence of nuclear spin-free silicon isotopes, e.g.,  $^{28}\text{Si}$ , allows isotopical enrichment in crystals<sup>3,4</sup>. Controlling individual electrons and spins in highly enriched  $^{28}\text{Si}$  quantum structures<sup>5–8</sup> then opens the door to an attractive spin qubit platform realized in a crystalline nuclear spin vacuum. Indeed, two-qubit gates<sup>9–12</sup> have recently been demonstrated in natural and enriched quantum films, while isotopical purification of  $^{28}\text{Si}$  down to 800 ppm of residual nuclear spin-carrying  $^{29}\text{Si}$  allowed to push manipulation fidelities beyond 99.9% for a single qubit<sup>13,14</sup> and towards 98% for two qubits<sup>15</sup>. Qubit manipulation of individual spins is currently either realized with local ac magnetic fields generated by a stripline to drive Rabi transitions<sup>6,7,16</sup> or via artificial spin-orbit coupling engineered by a micromagnet integrated into the device. This latter approach is advantageous by allowing the control of spin qubits solely by local ac electric fields<sup>10,11,13,17</sup>, permitting excellent local control and faster Rabi frequencies. At the same time, it opens a new dephasing channel for electric noise, due to the static longitudinal gradient magnetic field of the micromagnet, competing with the magnetic noise. To fully exploit the potential of magnetic noise minimization through isotope enrichment in  $^{28}\text{Si}/\text{SiGe}$ , two experimental questions thus become relevant for devices with integrated static magnetic field gradients: Firstly, to what extent electronic noise impacts the spin qubit dephasing compared to magnetic noise<sup>18</sup> and, secondly, which role the natural SiGe potential wall barriers play for dephasing, since the hyperfine interaction of bulk Ge exceeds the one of bulk Si by a factor of approximately 100<sup>19,20</sup>.

Here, we present an electron spin qubit implemented in a highly isotopically purified  $^{28}\text{Si}/\text{SiGe}$  device, the quantum well of which is grown with 60 ppm residual  $^{29}\text{Si}$  source material. It includes a magnetic field gradient generated by a nanomagnet which is integrated into the electron-confining device plane. We use Ramsey fringe experiments to investigate the splitting noise spectrum of the single electron spin down to  $10^{-5}$  Hz. We find the frequency dependence of the fluctuation spectrum of the qubit splitting to be identical to the spectrum of the device's electric charge noise over more than 8 decades. At low frequencies, below  $5 \cdot 10^{-3}$  Hz, both noise spectra decrease with  $1/f^2$ . Above, they transit to a  $1/f$  dependence as deduced from a Hahn-echo sequence for the detuning, yielding  $T_2^{\text{echo}} = 128 \mu\text{s}$ . From our observations, we conclude that electric noise dominates our qubit dephasing in a broad frequency range. It is also responsible for the observed decrease of  $T_2^*$  with increasing measurement time<sup>21</sup>. The high-frequency behavior is strikingly comparable to a device<sup>13</sup> which differs in its layout, magnet design, and heterostructure, including isotope purification. Interestingly, although we show the  $^{73}\text{Ge}$  in the quantum well-defining natural SiGe to represent a potential limitation for our device, our experiments suggest the nuclear spin bath to be frozen on a time scale of hours and to much less contribute to  $T_2^*$  than expected at the ergodic limit.

## RESULTS

The device used for all measurements consists of an undoped  $^{28}\text{Si}/\text{SiGe}$  heterostructure, confining a two-dimensional electron gas in  $^{28}\text{Si}$ . Metal gates allow to form a quantum dot (QD) containing a single electron (Fig. 1a). The charge state of the QD is detected via a single electron transistor (SET) located at the right-hand side of the device. The large gate labeled M on the left-hand side is a single domain cobalt nanomagnet. Its stray-magnetic field provides a magnetic field gradient<sup>22</sup> for spin driving by electric dipole spin resonance (EDSR). For details of the device see the

<sup>1</sup>JARA-FIT Institute for Quantum Information, Forschungszentrum Jülich GmbH and RWTH Aachen University, Aachen, Germany. <sup>2</sup>Institut für Experimentelle und Angewandte Physik, Universität Regensburg, Regensburg, Germany. <sup>3</sup>Advanced Research Laboratories, Tokyo City University, Tokyo, Japan. <sup>4</sup>Leibniz-Institut für Kristallzüchtung (IKZ), Berlin, Germany. <sup>5</sup>Institute of Physics, Polish Academy of Sciences, Warsaw, Poland. ✉email: dominique.bougeard@ur.de; lars.schreiber@physik.rwth-aachen.de

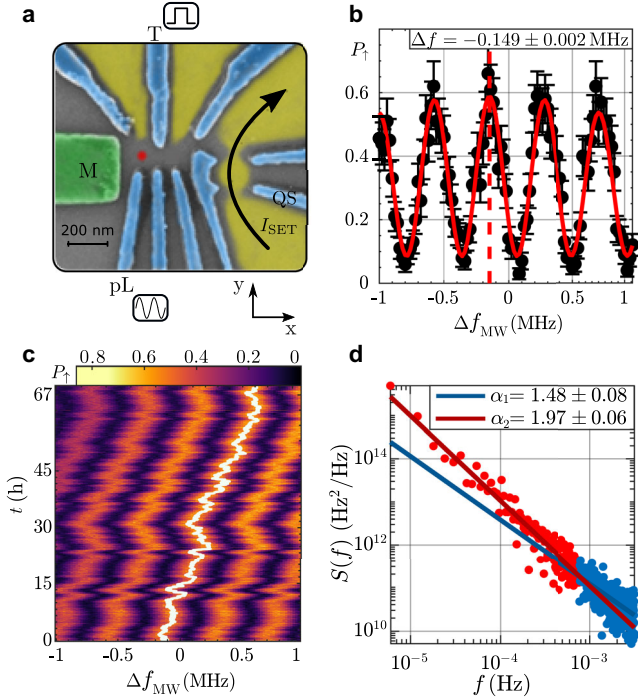


**Fig. 1** Qubit energy splitting noise. **a** Colored scanning electron micrograph of a sample similar to the one used in this work. **b** Measurement of Ramsey fringes. The spin-up probability  $P_{\uparrow}$  is recorded as a function of the resonance detuning  $\Delta f_{MW}$ . Each point corresponds to 100 single-shot measurements. The position of the spin resonance is indicated by the dashed red line. **c** Time evolution of the Ramsey fringe pattern during a measurement time  $t = 67$  h. The white solid line tracks the resonance detuning  $\Delta f$  extracted from the fringes. **d** PSD  $S(f)$  of the qubit detuning calculated from the data shown in panel (c). Error bars in panel (b) denote standard error.

“Methods” section and ref. <sup>23</sup>. We apply an external magnetic field of 668 mT along the  $x$ -direction.

Power spectral density of the qubit energy splitting noise

First, we focus on the power spectral density (PSD) of the frequency detuning  $\Delta f$  of the qubit with respect to a reference frequency of  $f_R = 19.9$  GHz.  $\Delta f$  is determined by a Ramsey fringe measurement, during which the microwave pulses are detuned from the reference by  $\Delta f_{MW}$  (Fig. 1b). We vary  $\Delta f_{MW}$  from  $-1$  to  $1$  MHz in 100 steps. Each point of the spin-up probability  $P_{\uparrow}$  is an average of over 100 single-shot measurements. One Ramsey fringe, which is one measurement of  $\Delta f$ , takes 120 s. We fit  $\Delta f$  by applying the formula for the fringe pattern<sup>24</sup>:

$$P_{\uparrow}(f_R, t_e, \Delta f, t_{\frac{\pi}{2}}) = A \cdot \frac{4f_R^2}{\Phi^2} \cdot \sin\left(\pi t_{\frac{\pi}{2}} \Phi\right)^2 \cdot \left[ \cos(\pi \Delta f t_e) \cos\left(\pi t_{\frac{\pi}{2}} \Phi\right) - \frac{\Delta f}{\Phi} \sin(\pi \Delta f t_e) \sin\left(\pi t_{\frac{\pi}{2}} \Phi\right) \right]^2 + B \quad (1)$$

where  $\Phi = \sqrt{\Delta f^2 + f_R^2}$ ,  $t_e$  is the evolution time between the two  $\pi/2$  gates, and  $t_{\frac{\pi}{2}}$  is the execution time of the  $\pi/2$  gate.  $A$  and  $B$  are constants related to the qubit initialization and readout fidelity.

Figure 1c displays Ramsey fringes recorded during a measurement time  $t$  of 67 h. The white line tracks  $\Delta f$  during the full-time period. We calculated the PSD  $S(f)$  of the qubit detuning with Welch’s method (Fig. 1d). For frequencies below  $\approx 7 \cdot 10^{-4}$  Hz, we find a  $S(f) \propto 1/f^{1.97}$  dependence. It transitions into a region with a smaller exponent, here fitted with  $S(f) \propto 1/f^{1.48}$  (blue line in Fig. 1d). Note that the slow drift towards increasing  $\Delta f$  in Fig. 1c cannot be induced by a discharge of the magnet in persistent mode, which

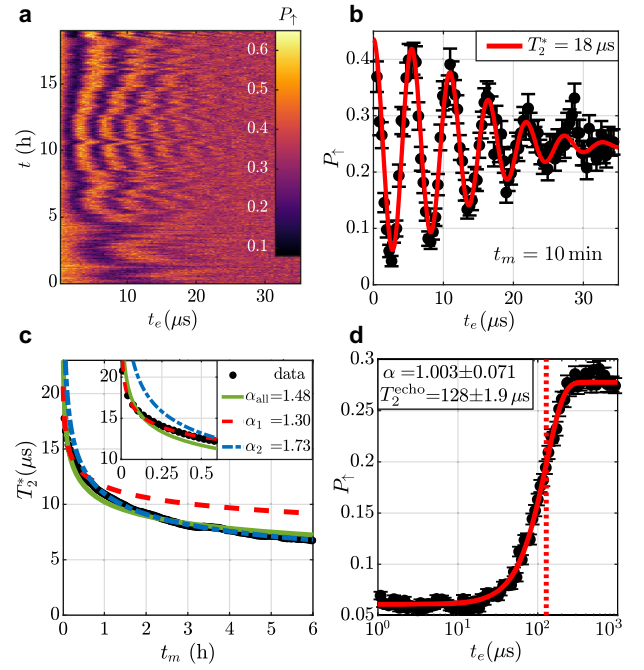


**Fig. 2** Spin dephasing time  $T_2^*$  via Ramsey fringes. **a** Time evolution of the  $T_2^*$  measurement. Each point is an average of over 50 single-shot measurements. **b** Measurement of the spin-up probability as a function of the evolution time  $t_e$ . Each point corresponds to 500 single-shot measurements. The solid line shows a fit of a Gaussian decay revealing the time-ensemble dephasing time  $T_2^*$ . **c** Dependence of  $T_2^*$  on the measurement time. The solid green line shows a fit to all data points with one  $\alpha$ -value. The dashed red and blue lines show fits to only a part of the data points: the shorter (dashed red) and longer (dashed blue) measurement times. **d** Spin-up probability as a function of the evolution time  $t_e$  after a Hahn-echo gate sequence. Each point is an average of over 5000 single-shot measurements. The solid line is a fit to Eq. (4). The dotted line marks the fitted  $T_2^{\text{echo}}$ . Error bars in panels (b) and (d) denote standard error.

would lead to a decreased energy splitting. It only appears when manipulating the qubit and is captured at most in the two lowest frequencies in the PSD in Fig. 1d.

Time-averaged spin dephasing time  $T_2^*$

Having analyzed the qubit splitting noise  $S(f)$  in the low-frequency regime, we now investigate its impact on the time-ensemble spin dephasing time  $T_2^*$ . Starting at a lab time  $t$ , we record  $P_{\uparrow}$  during a series of Ramsey sequences with varying  $t_e$  (Fig. 2a) in every line. We average as many consecutive  $P_{\uparrow}(t_e)$  lines of this dataset as required to reach a total measurement time  $t_m$ . The averaged  $P_{\uparrow}(t_e)$  is fitted with

$$P_{\uparrow}(t_e) = A \cdot \exp\left(-\left(\frac{t_e}{T_2^*}\right)^2\right) \cos(2\pi \Delta f \cdot t_e) + B, \quad (2)$$

An example of  $P_{\uparrow}(t_e)$  averaged from a bundle of  $P_{\uparrow}(t_e)$  lines measured over  $t_m = 10$  min, starting at lab time  $t \approx 10$  h, is shown in Fig. 2b. We extract  $T_2^*(t_m = 10 \text{ min}) = 18 \mu\text{s}$ . To achieve better statistics, this procedure was executed consecutively for different bundles, i.e., different lab times  $t$ . We choose to offset the bundles by 25 lines giving overlap between them. This results in each  $T_2^*(t_m)$  value being averaged from 900  $T_2^*(t_m)$  values, using different line bundles from the dataset displayed in Fig. 2a and a second dataset not shown here. Figure 2c shows these averaged  $T_2^*(t_m)$  for  $t_m$  ranging between 38 s and 6.3 h. Remarkably,  $T_2^*(t_m)$  drops monotonously with increasing measurement time without

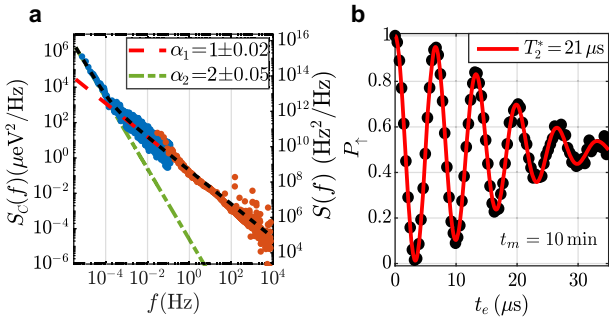


**Fig. 3** Charge noise of the spin qubit device. **a** PSD of the charge noise determined by the noise of the current  $I_{\text{SET}}$  through the SET. The blue and the red dots represent two datasets. We read  $S_C^{1/2}(1 \text{ Hz}) = 0.47 \mu\text{eV}/\sqrt{\text{Hz}}$  at 1 Hz. The right y-axis is converted into the PSD scale of splitting noise by Eq. (5). **b** Simulation of the spin-up probability  $P_1$  as a function of the evolution time  $t_e$  taking the measured charge noise spectrum into account (black dots).  $T_2^*$  is fitted (red line) by the same fit function as in Fig. 2b.

saturation for long  $t_m$ , qualitatively matching the qubit splitting noise PSD  $S(f)$ , which keeps increasing towards low frequencies (Fig. 1d). In a rough approximation, considering splitting noise of the type  $S(f) = S_0/f^\alpha$  with  $\alpha \gtrsim 1$ ,  $T_2^*(t_m)$  induced by splitting noise is (see “Methods”):

$$T_2^*(t_m) = \left( \frac{4\pi^2 S_0}{\alpha - 1} (t_m^{\alpha-1} - t_e^{\alpha-1}) \right)^{-\frac{1}{\alpha}}. \quad (3)$$

Fitting  $T_2^*(t_m)$  with only one  $\alpha_{\text{all}} = 1.48$  (green solid line) shows a clear deviation from the data points (Fig. 2c). Motivated by the variation of  $\alpha$  in  $S(f)$  observed in Fig. 1d, we fit two separate ranges of  $t_m$  above and below  $t_m = 25 \text{ min}$  (that is  $6.7 \cdot 10^{-4} \text{ Hz}$ , which is very close to the transition point  $7 \cdot 10^{-4} \text{ Hz}$  found in Fig. 1d). These ranges are characterized by  $\alpha_1 = 1.30$  (red dashed curve) and  $\alpha_2 = 1.73$  (blue dashed curve), and are thus in good qualitative agreement with the exponents found for the splitting noise in Fig. 1d. The quantitative deviation of both  $\alpha_i$  ( $i = 1, 2$ ) determined by the  $T_2^*(t_m)$  compared to the exponents of the fits to the PSD results from the fact that the  $T_2^*$  measurement integrates over the PSD from  $t_m^{-1}$  to  $t_e^{-1}$ .

#### Hahn-echo spin dephasing time $T_2^{\text{echo}}$

Our spin-detection bandwidth in the Ramsey fringe experiment sets a limit on the maximum frequency of  $S(f)$  in Fig. 1d. To gain information on  $S(f)$  at a higher frequency, we perform a Hahn-echo experiment, that extends the Ramsey control sequence by a  $\pi_x$  gate between the two  $(\pi/2)_x$  gates, in order to filter out low-frequency noise. The measured data (Fig. 2d) is fitted with

$$P_1(t_e) = A \cdot \left( 1 - \exp\left(-\left(\frac{t_e}{T_2^{\text{echo}}}\right)^{\alpha+1}\right) \right) + B. \quad (4)$$

We find  $\alpha = 1.003 \pm 0.071$  and  $T_2^{\text{echo}} = 128 \pm 1.9 \mu\text{s}$ . We can deduce that  $S(f) \propto 1/f$  at a frequency of approximately  $f = 1/T_2^{\text{echo}} = 7.8 \text{ kHz}$ , in line with the observations in a device with an on-chip micromagnet and 800 ppm residual  $^{29}\text{Si}$  for  $f > 10^{-2} \text{ Hz}^{13}$ . With the low-frequency PSD (Fig. 1d) and these spin echo results, we conclude that the initial  $S(f) \propto 1/f^2$  dependence observed at low frequencies transits to a  $S(f) \propto 1/f$  dependence around  $7 \cdot 10^{-4}$ – $1 \cdot 10^{-3} \text{ Hz}$ . With the detection bandwidth limit set by the Ramsey fringe experiment at approximately  $3 \cdot 10^{-3} \text{ Hz}$ , we observe this gradual transition in our study, explaining  $\alpha = 1.48$  found in Fig. 1d. Remarkably, we find a 28% higher  $T_2^{\text{echo}}$  compared to the device with an on-chip micromagnet and 800 ppm residual  $^{29}\text{Si}^{13}$ , indicating that overall the splitting noise is lower in our sample in this regime.

#### Power spectral density of charge noise

In order to investigate the impact of charge noise, we measure the charge noise in the qubit vicinity via the current noise of the SET sensor. This current noise is translated into gate equivalent voltage-noise by the variation  $dI_{\text{SET}}/dV_{\text{QS}}$  of the SET current by the voltage applied to the SET gate QS (see Fig. 1a). We measure the current noise  $\epsilon_{\text{SET}}$  at a highly sensitive operation point of the SET and subtract from its PSD the noise spectrum measured when the SET is set to be insensitive to charge noise from the device, in order to remove noise originating from the measurement circuit<sup>25</sup>. Figure 3a shows the measured PSD of the SET noise. As the data reveals two slopes, we fit with  $S_C(f) = S_{C1}/f^{\alpha_1} + S_{C2}/f^{\alpha_2}$ . The fitted exponents of the  $S_C(f)$  spectrum are  $\alpha_1 = 1 \pm 0.02$  and  $\alpha_2 = 2 \pm 0.05$ , respectively, the transition being at about  $10^{-3} \text{ Hz}$ . This frequency dependence is in very good agreement with the one observed for the qubit detuning PSD in Fig. 1d and with the qualitative trend extended to high frequencies with the Hahn-echo experiment. Note that spin qubits in GaAs which dephase dominantly due to hyperfine interaction<sup>26–28</sup> are also characterized by a  $1/f^2$  dependence in their low-frequency splitting noise PSD, which has been assigned to nuclear spin diffusion there<sup>29,30</sup>. As discussed in the next section, nuclear spin diffusion seems implausible in our structure. It seems more likely that the appearance of the low-frequency  $\alpha_2 = 2 \pm 0.05$  is due to a high density of two-level charge fluctuators with very low switching rates.

To provide a quantitative estimation, we assume the charge noise at the SET to be similar to the one of the QD and the longitudinal gradient magnetic field to be isotropic for lateral QD displacements. Using the current noise trace  $\epsilon_{\text{SET}}(t)$ , the resulting frequency detuning is

$$\Delta f(t) = \epsilon_{\text{SET}}(t) \cdot \frac{dV_{\text{QS}}}{dI_{\text{SET}}} \cdot \frac{dx_{\text{QD}}}{dV_{\text{QD}}} \cdot \frac{dB_x}{dx_{\text{QD}}} \cdot \frac{g\mu_B}{\hbar}, \quad (5)$$

where  $\frac{dV_{\text{QS}}}{dI_{\text{SET}}} = \frac{1}{35} \text{ mV/pA}$  is the inverse of the current change through the SET induced by a change of the voltage on the gate.  $\frac{dx_{\text{QD}}}{dV_{\text{QD}}} = 0.024 \text{ nm/mV}$  is the estimated displacement of the QD induced by voltage changes on the adjacent gates, represented by gate-equivalent uncorrelated charge-noise applied to gate pL deduced from an electrostatic device simulation.  $\frac{dB_x}{dx_{\text{QD}}} = 0.08 \text{ mT/nm}$  is the simulated isotropic longitudinal gradient magnetic field at the QD position. The factor  $\frac{g\mu_B}{\hbar}$ , containing the electron  $g$ -factor ( $g \approx 2$ ), the Bohr magneton  $\mu_B$ , and the reduced Planck constant  $\hbar$ , converts magnetic field to frequency. We convert the charge noise PSD into qubit splitting noise by Eq. (5) (right y-axis in Fig. 3a). We find this noise-power to vary by a factor of three, depending on the assumptions on the gate-to-dot distance and the direction of displacement triggered by the gate, an error which is small on the scale covered in Fig. 3a. Comparing the experiment and the quantitative estimation, the low-frequency part of the PSD (blue dots in Fig. 3a) shows excellent agreement with the qubit splitting noise PSD  $S(f)$  in its frequency dependence and its magnitude.

In order to also include the high-frequency range (red dots in Fig. 3a) into the comparison, we simulated the spin-up probability after a Ramsey gate sequence with evolution time  $t_e$  using

$$P_1(t, t_e) = \frac{1}{2} (\cos(2\pi t_e \Delta f(t)) + 1) \quad (6)$$

and included quasi-static noise during the free evolution time  $t_e$  from the full PSD in Fig. 3a. The simulated data points (black dots in Fig. 3b) yield  $T_2^* = 21 \mu\text{s}$  for a measurement time  $t_m = 10 \text{ min}$ . Note that this estimated  $T_2^*$  value is surprisingly close to the experimentally determined value  $T_2^* = 18 \mu\text{s}$  found in Fig. 2b, given that the above-mentioned accuracy of the qubit energy-splitting noise-power estimation enters with  $\sqrt{3}$  into the estimation of  $T_2^*$ .

In summary, comparing data covering more than 8 frequency decades, the excellent agreement demonstrates that charge noise dominates the qubit splitting noise in our device and transmits from a  $S(f) \propto 1/f^2$  dependence to a  $S(f) \propto 1/f$  dependence around  $10^{-3}$  Hz.

#### Contact hyperfine interaction analysis

To complete our analysis of the splitting noise and the time-ensemble spin dephasing time  $T_2^*$ , we estimate the magnetic noise impact due to the residual non-zero spin nuclei in our device. We can compute the resulting  $T_2^*$  with (see “Methods”)

$$T_2^* = \frac{\hbar\sqrt{3N_S}}{p\gamma A\sqrt{2I(I+1)}}, \quad (7)$$

where  $N_S$  is the number of nuclei,  $p$  is the fraction of nuclei with finite nuclear spin,  $\gamma$  is the volume fraction of the wavefunction for which we want to calculate the influence on  $T_2^*$ , i.e., localized in the barrier or the quantum well.  $A$  is the hyperfine coupling constant per nucleus and  $I$  is the non-zero nuclear spin. In ref. <sup>23</sup>, we measured the orbital splitting of this QD to be 2.5 meV. Assuming a harmonic potential, we calculate the size of the QD, taken to be the full-width-at-half-maximum of the ground state wavefunction. This yields a radius of  $\approx 13$  nm. By approximating the QD as a cylinder with height 6 nm we estimate the number of atoms in the QD volume to be  $N_A = 1.6 \cdot 10^5$ . From Schrödinger–Poisson simulations, we estimate the overlap with the SiGe barriers to be  $\gamma_B \approx 0.1\%$ . We calculate the number of non-zero nuclear spins, which are relevant for the hyperfine coupling with the qubit (i.e., are within the cylindrical volume assigned to the QD), for the minimal residual concentration of 60 ppm  $^{29}\text{Si}$  in the  $^{28}\text{Si}$  strained QW layer, residual  $^{29}\text{Si}$  and  $^{73}\text{Ge}$  in the SiGe barriers with natural abundance of isotopes as, respectively:

$$N_{S,^{29}\text{Si}}^{\text{QW}} = p_{^{29}\text{Si}}^{\text{QW}}(1 - \gamma_B)N_A = 60 \cdot 10^{-6}(1 - \gamma_B)N_A \approx 9.6, \quad (8)$$

$$N_{S,^{29}\text{Si}}^{\text{barrier}} = p_{^{29}\text{Si}}^{\text{barrier}}\gamma_B N_A = 0.0467 \cdot 0.7 \cdot \gamma_B N_A \approx 5.2, \quad (9)$$

$$N_{S,^{73}\text{Ge}}^{\text{barrier}} = p_{^{73}\text{Ge}}^{\text{barrier}}\gamma_B N_A = 0.0776 \cdot 0.3 \cdot \gamma_B N_A \approx 3.7. \quad (10)$$

The coupling constants are  $A_{\text{Si}} = 2.15 \mu\text{eV}$  and  $A_{\text{Ge}} \approx 10 \cdot A_{\text{Si}}$ <sup>19,20</sup>, respectively, with  $I_{^{29}\text{Si}} = \frac{1}{2}$ ,  $I_{^{73}\text{Ge}} = \frac{3}{2}$ . Assuming the spin baths to be in the ergodic limit, each subset of nuclear spin results in the following dephasing times:  $T_2^*(^{29}\text{Si}^{\text{QW}}) = 22 \mu\text{s}$ ,  $T_2^*(^{29}\text{Si}^{\text{barrier}}) = 30 \mu\text{s}$ , and  $T_2^*(^{73}\text{Ge}^{\text{barrier}}) = 0.61 \mu\text{s}$ .

At first sight, it seems striking that  $T_2^*(^{29}\text{Si}^{\text{QW}})$  coincides with our experimental observation, but this only holds true for the shortest  $t_m$  in Fig. 2c. Attributing the dephasing solely to  $^{29}\text{Si}$  would require the dephasing channel due to  $^{73}\text{Ge}$  nuclei to be negligible and imply the implausible conclusion that the experimental matching of the PSDs of the magnetic and the charge noise is a simple coincidence. Additionally, ref. <sup>13</sup> reports the same  $T_2^*$  for the same measurement time in a heterostructure with 800 ppm  $^{29}\text{Si}$ . The observed  $S(f) \propto 1/f^2$  in Fig. 1d by itself could be the high-frequency tail of nuclear PSD (as observed for GaAs) for nuclei having extremely long correlation time. But this is extremely unlikely considering the total magnitude of the PSD. If the  $S(f) \propto 1/f^2$  region was dominated by  $^{29}\text{Si}$ , it would imply the ergodic limit of  $T_2^*$  to be reached for  $t_m$  even longer than the highest values reported here. But then, according to Fig. 2c, the nuclear-induced  $T_2^*$  in the ergodic limit would be at most a few microseconds, in disagreement with  $>20 \mu\text{s}$  calculated for  $^{29}\text{Si}$ . This leads us to rule out a dominant dephasing through  $^{29}\text{Si}$ .

Notably, due to the strong hyperfine coupling of the  $^{73}\text{Ge}$  in the barrier layers, the  $^{73}\text{Ge}$  alone would dephase the qubit faster than observed in the experiment shown in Fig. 2c. This apparent contradiction would be resolved if the correlation time of the  $^{73}\text{Ge}$  nuclear spin bath is larger than our measurement time of 6 h and thus the ergodic limit is not reached in our  $T_2^*(t_m)$  measurement.

The gradient magnetic field of the nanomagnet and the presence of the electron’s Knight shift<sup>31</sup> may contribute to this effect of slowing down the nuclear spin diffusion.

## DISCUSSION

We have shown that in a highly purified  $^{28}\text{Si}/\text{SiGe}$  qubit device grown from 60 ppm residual  $^{29}\text{Si}$  source material, the natural abundance of  $^{73}\text{Ge}$  nuclear spins in the potential barrier does not seem to dominantly contribute to the qubit dephasing time, despite their strong hyperfine coupling. One can thus conclude that, in this scenario, the improvement potential of qubit dephasing times that can be expected from an isotopical purification of the natural SiGe barrier of the heterostructure will be negligibly small.

In our device featuring a nanomagnet integrated into the gate layout for EDSR manipulation, we demonstrate charge noise to be the dominant qubit noise source in a frequency range of more than 8 decades by comparing the qubit energy splitting noise to the charge noise of the sensor SET. In the low-frequency regime, the charge and the qubit splitting noise present an unexpected  $1/f^2$  dependence below  $1 \cdot 10^{-3}$  Hz. Above, towards higher frequencies, both PSD transit to a  $1/f$  dependence. This  $1/f$  trend was recently also observed in a different type of device, featuring a micromagnet and 800 ppm  $^{29}\text{Si}$ <sup>13</sup>. From the Hahn-echo experiment for our qubit detuning, we additionally deduce a remarkably high  $T_2^{\text{echo}} = 128 \mu\text{s}$ . In accordance with the absence of a roll-off in the charge noise PSD down to at least  $5 \cdot 10^{-5}$  Hz, we also show  $T_2^*$  to clearly and monotonously decrease for the measurement time which we increased from seconds to several hours. Our experimental  $T_2^* \approx 18 \mu\text{s}$  for a measurement time  $t_m = 600$  s quantitatively results from the charge noise  $S_C^{1/2}(1 \text{ Hz}) = 0.47 \mu\text{eV}/\sqrt{\text{Hz}}$ , which falls within the range of  $0.3\text{--}2 \mu\text{eV}/\sqrt{\text{Hz}}$  seen in literature<sup>32–35</sup>. While the on-chip integration of a micro- or nanomagnet does not induce additional magnetic noise<sup>13,36</sup>, minimizing the newly opened electric dephasing channel seems to be key for further significant improvement of spin qubit gate fidelities in highly purified  $^{28}\text{Si}$ , compared to devices avoiding integrated static magnetic field gradients<sup>14,15,37,38</sup>.

## METHODS

### Device

The device studied in this work is fabricated with an undoped  $^{28}\text{Si}/\text{SiGe}$  heterostructure<sup>23</sup>. The layer structure is grown on a Si-wafer by means of a solid source molecular beam epitaxy. A relaxed virtual substrate consisting of a graded buffer up to a composition  $\text{Si}_{0.7}\text{Ge}_{0.3}$  followed by a layer of constant composition  $\text{Si}_{0.7}\text{Ge}_{0.3}$  provides the basis for a 12 nm  $^{28}\text{Si}$  quantum well (QW) grown using a source material of isotopically purified  $^{28}\text{Si}$  with 60 ppm of remaining  $^{29}\text{Si}$ . The QW is separated from the interface by a 45 nm  $\text{Si}_{0.7}\text{Ge}_{0.3}$  cap, which is protected from oxidation by a 1.5 nm Si cap.

A layer of 20 nm  $\text{Al}_2\text{O}_3$  grown by atomic layer deposition insulates the depletion gate layer depicted in Fig. 1a and the underlying heterostructure. The depletion gates are fabricated by means of electron beam lithography. A Co nanomagnet, colored green in Fig. 1a, is added to the depletion gate layer in order to provide a local magnetic field gradient for electric dipole spin resonance (EDSR). A second gate layer, insulated from the depletion gates by 80 nm of  $\text{Al}_2\text{O}_3$ , is used to induce a two-dimensional electron gas in the QW via the field effect and provide reservoirs for the dot-defining and charge sensing parts of the device.

### Setup

The device was measured in an Oxford Triton dilution refrigerator at a base temperature of 40 mK. All dc lines are heavily filtered using pi-filters ( $f_c = 5$  MHz) at room temperature followed by copper-powder filters and a second-order RC low-pass filter at base temperature. The RC filter cut-off frequency is  $f_c = 10$  kHz for the electron reservoirs and gates that are used

for fast control. All other gates have a RC low-pass filter cut-off frequency of  $\sim 0.68$  kHz. The copper-powder filter has an attenuation of 60 and 80 dB at 3 and 12 GHz, respectively. The electron temperature is 114 mK. Voltage pulses are applied via a Tabor Electronics WX2184C AWG. MW manipulation bursts for control are provided by a Rohde & Schwarz SMW200A signal source. MW signals can be added to the pL gate via a resistive bias-tee. The sensor signal for read-out is amplified with a Basel high stability  $I-V$  converter SP983C at room-temperature. The resulting voltage signal is digitized with an AlazarTech ATS9440 digitizer card.

Derivation of the measurement time dependence of  $T_2^*$

Using the qubit coherence function  $W(t_e)$  as defined in ref. <sup>39</sup>, we can approximate the dephasing due to splitting noise for noise models of the type  $S(f) = S_0/f^\alpha$  with  $\alpha \geq 1$  as

$$W(t_e) \equiv e^{-\chi(t_e)} = \exp\left(-4\pi^2 \int_0^\infty S(f) \frac{2F_{t_e}(f)}{f^2} df\right) \approx e^{-\left(\frac{t_e}{T_2^*}\right)^2}. \quad (11)$$

For low frequencies,  $F_{\text{FID}}/f^2 \approx \frac{1}{2}t_e^2$  and thus for measurement times  $t_m \gg t_e$

$$\int_0^\infty S(f) \frac{2F_{\text{FID}}(f)}{f^2} df = \int_{t_m^{-1}}^{t_e^{-1}} \frac{S_0 t_e^2}{f^4} df \quad (12)$$

When plugged into the expression for  $W(t_e)$ , this gives us the relation

$$\left(\frac{t_e}{T_2^*}\right)^2 = \frac{4\pi^2 S_0 t_e^2}{1-\alpha} (t_m^{\alpha-1} - t_e^{\alpha-1}). \quad (13)$$

Thus, we get an expression for the dephasing time constant

$$T_2^* = \left(\frac{4\pi^2 S_0}{\alpha-1} (t_m^{\alpha-1} - t_e^{\alpha-1})\right)^{-\frac{1}{2}}. \quad (14)$$

Derivation of the nuclear bath induced  $T_2^*$  formula

The wavefunction of the confined electron is given in the envelope function approximation by

$$\Psi(\mathbf{r}) = F(\mathbf{r})u(\mathbf{r}), \quad (15)$$

where  $F(\mathbf{r})$  is the slowly varying envelope function and  $u(\mathbf{r})$  is the periodic part of the Bloch function. The envelope function  $F(\mathbf{r})$  is normalized to the volume of the primitive unit cell of silicon

$$\int |F(\mathbf{r})|^2 d^3\mathbf{r} = \nu_0, \quad (16)$$

where the volume of the primitive unit cell is

$$\nu_0 = \frac{a^3}{4} \quad (17)$$

in which  $a$  is the lattice constant of Si. Here we have taken into account that in a cubic unit cell we have eight atoms while in the primitive unit cell of a diamond-type lattice we have two atoms. So the volume of the primitive cell is 1/4 of the volume of the cubic unit cell. Since the envelope in the  $n$ th primitive unit cell (PUC) is approximately constant, given by  $F_n$ , we have

$$\nu_0 = \int |F(\mathbf{r})|^2 d^3\mathbf{r} = \nu_0 \sum_{n \in \text{PUC}} |F_n|^2. \quad (18)$$

Thus,

$$\sum_{n \in \text{PUC}} |F_n|^2 = 1 \quad (19)$$

Since the whole wavefunction is normalized to unity we can write

$$1 = \int |\Psi(\mathbf{r})|^2 d^3\mathbf{r} \approx \sum_{n \in \text{PUC}} |F_n|^2 \int_{\nu_0} |u(\mathbf{r})|^2 d^3\mathbf{r}, \quad (20)$$

from which we get

$$\int_{\nu_0} |u(\mathbf{r})|^2 d^3\mathbf{r} = 1 \quad (21)$$

meaning  $\nu_0 |u(\mathbf{r}_k)|^2$  is a dimensionless quantity (denoted by  $\eta$  in ref. <sup>2</sup>)

The hyperfine (hf) coupling Hamiltonian is

$$H_{\text{hf}} = \sum_k A_k \mathbf{S} \cdot \mathbf{I}_k, \quad (22)$$

where  $k$  labels the spinful atoms and  $A_k$  is the hf coupling to the  $k$ th nucleus. Note that at magnetic fields along the  $z$ -axis being much larger than typical Overhauser fields from all the nuclei, we can neglect the transversal couplings in the above Hamiltonian and just consider  $S^z I^z$  interaction.

The hf coupling with a nuclear spin located at  $\mathbf{r}_k$  is given by

$$A_k = \mathcal{A} |F(\mathbf{r}_k)|^2, \quad (23)$$

where  $\mathcal{A}$  is the hf coupling energy of one nucleus. It is related to gyromagnetic factors of the electron and nucleus and to the amplitude of the Bloch function at the nuclear site  $|u(\mathbf{r})|^2$ .

Let us note that due to the normalization of  $F$  discussed above the sum over all the  $A_k$  is

$$\sum_k A_k \approx 2p\mathcal{A} \sum_n |F_n|^2 = 2p\mathcal{A}, \quad (24)$$

where  $p$  is the fraction of nuclei with a nuclear spin, e.g.,  $p = 0.049$  for natural Si. The factor of 2 comes from the fact that we have two atoms per PUC. For Silicon  $\mathcal{A} \approx 2.15$   $\mu\text{eV}$

The rms value of the Overhauser field for unpolarized nuclei is given by<sup>28</sup>

$$\sigma^2 = \frac{1}{3} I(I+1) \sum_k A_k^2. \quad (25)$$

We now define the number of primitive unit cells encompassed by the wavefunction as<sup>27</sup>

$$N \equiv \frac{\sum_n |F_n|^2}{\sum_n |F_n|^4} = \frac{1}{|F_n|^4}, \quad (26)$$

from which we get that

$$\sum_k A_k^2 = 2p\gamma \sum_n A_n^2 = \frac{2p\gamma \mathcal{A}^2}{N}. \quad (27)$$

Here  $\gamma$  is the volume fraction of the electron wavefunction, in which the nuclei are positioned, for which we calculate the influence on  $T_2^*$  of the electron spin. From this we get

$$\sigma = \sqrt{\frac{I(I+1)}{3}} \frac{\sqrt{2p\gamma} \mathcal{A}}{N}. \quad (28)$$

We can rewrite this formula using the number of spins in a QD,  $N_S = 2p\gamma N$

$$T_2^* = \frac{\hbar \sqrt{3N_S}}{p\gamma \mathcal{A} \sqrt{2I(I+1)}}. \quad (29)$$

Measurement cycle and magnetic field gradient

The measurement cycle (Fig. 4a) starts with a 1 ms long Ramsey pulse sequence, during which two  $\left(\frac{\pi}{2}\right)_x$  qubit-gates separated by the evolution time  $t_e$  are generated by applying microwave pulses to gate pL (see Fig. 1a). The microwave pulses, which can be detuned from spin resonance by  $\Delta f_{\text{MW}}$ , displace the QD and thus drive EDSR in Coulomb blockade. The Ramsey sequence is followed by a measurement voltage pulse applied to gate T, during which the electron spin state projected on the external magnetic field direction is detected by spin-dependent tunneling to the reservoir and the QD is initialized in the spin ground state. This sequence containing initialization, control, and single-shot readout is repeated 100 times, with either the frequency  $\Delta f_{\text{MW}}$  or the evolution time  $t_e$  varied in each Ramsey sequence. This sequence is looped five times and followed by a pulse sequence designed to calibrate the chemical potential  $\mu_{\text{QD}}$  of the QD, the tunnel-coupling to the reservoir  $t_c$ , and the operation point of the SET. The calibration sequence starts with 40 voltage ramps applied to gate T (20 up and 20 down) crossing the 0–1 charge transition and thus calibrating  $\mu_{\text{QD}}$  of the spin ground-state as a function of  $V_T$ . During the second part of the calibration pulse,  $V_T$  is held constant for 20 ms and the time for loading an electron on the QD in its spin-ground state is observed, in order to update  $t_c$  and the sensitive operation point of the SET by averaging several calibration sequences. The whole initialization, Ramsey, spin-detection, and calibration sequence is repeated  $N$  times.

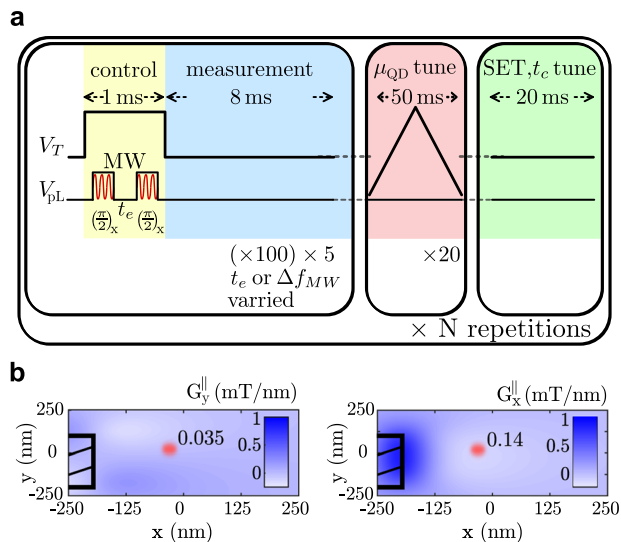


**Fig. 4** Qubit manipulation sequence in a magnetic field gradient. **a** Schematic overview of the initialization, Ramsey, spin detection, and calibration sequence. During the sequence, the voltage  $V_T$  applied to gate T is pulsed and microwaves (MW) pulses are applied to gate pL. **b** Simulation of the magnetic field gradient within the 2DEG due to the Co nanomagnet M. The longitudinal magnetic gradient of the dot displacement along the  $y$ - and  $x$ -direction is displayed by the left and right panel, respectively. The QD position is indicated by a red dot.

Simulations of the longitudinal gradient magnetic field generated by the Co nanomagnet in the plane of the Si/SiGe quantum well are displayed in Fig. 4b.

## DATA AVAILABILITY

The data sets generated and/or analyzed during this study are available from the corresponding author upon reasonable request.

Received: 4 October 2019; Accepted: 3 April 2020;

Published online: 15 May 2020

## REFERENCES

- Zwanenburg, F. A. et al. Silicon quantum electronics. *Rev. Mod. Phys.* **85**, 961–1019 (2013).
- Assali, L. V. C. et al. Hyperfine interactions in silicon quantum dots. *Phys. Rev. B* **83**, 165301 (2011).
- Ambrosimov, N. V. et al. A new generation of 99.999% enriched  $^{28}\text{Si}$  single crystals for the determination of Avogadro's constant. *Metrologia* **54**, 599–609 (2017).
- Itoh, K. M. & Watanabe, H. Isotope engineering of silicon and diamond for quantum computing and sensing applications. *MRS Commun.* **4**, 143 (2014).
- Wild, A. et al. Few electron double quantum dot in an isotopically purified  $^{28}\text{Si}$  quantum well. *Appl. Phys. Lett.* **100**, 143110 (2012).
- Muhonen, J. T. et al. Storing quantum information for 30 seconds in a nanoelectronic device. *Nat. Nanotechnol.* **9**, 986–991 (2014).
- Veldhorst, M. et al. An addressable quantum dot qubit with fault-tolerant control-fidelity. *Nat. Nanotechnol.* **9**, 981–985 (2014).
- Lawrie, W. I. L. et al. Quantum dot arrays in silicon and germanium. *Appl. Phys. Lett.* **116**, 080501 (2020).
- Veldhorst, M. et al. A two-qubit logic gate in silicon. *Nature* **526**, 410–414 (2015).
- Zajac, D. M. et al. Resonantly driven CNOT gate for electron spins. *Science* **359**, 439–442 (2018).
- Watson, T. F. et al. A programmable two-qubit quantum processor in silicon. *Nature* **555**, 633–637 (2018).
- He, Y. et al. A two-qubit gate between phosphorus donor electrons in silicon. *Nature* **571**, 371–375 (2019).

- Yoneda, J. et al. A quantum-dot spin qubit with coherence limited by charge noise and fidelity higher than 99.9%. *Nat. Nanotechnol.* **13**, 102–106 (2018).
- Yang, C. H. et al. Silicon qubit fidelities approaching incoherent noise limits via pulse engineering. *Nat. Electron.* **2**, 151 (2019).
- Huang, W. et al. Fidelity benchmarks for two-qubit gates in silicon. *Nature* **569**, 532–536 (2019).
- Koppens, F. H. L. et al. Driven coherent oscillations of a single electron spin in a quantum dot. *Nature* **442**, 766–771 (2006).
- Pioro-Ladrière, M. et al. Electrically driven single-electron spin resonance in a slanting Zeeman field. *Nat. Phys.* **4**, 776–779 (2008).
- Zhao, R. et al. Single-spin qubits in isotopically enriched silicon at low magnetic field. *Nat. Commun.* **10**, 5500 (2019).
- Wilson, D. K. Electron spin resonance experiments on shallow donors in germanium. *Phys. Rev.* **134**, A265–A286 (1964).
- Witzel, W. M., Rahman, R. & Carroll, M. S. Nuclear spin induced decoherence of a quantum dot in Si confined at a SiGe interface: decoherence dependence on  $^{73}\text{Ge}$ . *Phys. Rev. B* **85**, 205312 (2012).
- Dial, O. E. et al. Charge noise spectroscopy using coherent exchange oscillations in a singlet-triplet qubit. *Phys. Rev. Lett.* **110**, 146804 (2013).
- Petersen, G. et al. Large nuclear spin polarization in gate-defined quantum dots using a single-domain nanomagnet. *Phys. Rev. Lett.* **110**, 177602 (2013).
- Hollmann, A. et al. Large, tunable valley splitting and single-spin relaxation in a Si/Si<sub>0.8</sub>Ge<sub>0.2</sub> quantum dot. *Phys. Rev. Appl.* **13**, 034068 (2020).
- Lu, J. et al. High-resolution electrical detection of free induction decay and Hahn echoes in phosphorus-doped silicon. *Phys. Rev. B* **83**, 235201 (2011).
- Takeda, K. et al. Characterization and suppression of low-frequency noise in Si/SiGe quantum point contacts and quantum dots. *Appl. Phys. Lett.* **102**, 123113 (2013).
- Hanson, R., Kouwenhoven, L. P., Petta, J. R., Tarucha, S. & Vandersypen, L. M. K. Spins in few-electron quantum dots. *Rev. Mod. Phys.* **79**, 1217–1265 (2007).
- Cywiński, Ł., Witzel, W. M. & Das Sarma, S. Electron spin dephasing due to hyperfine interactions with a nuclear spin bath. *Phys. Rev. Lett.* **102**, 057601 (2009).
- Cywiński, Ł. Dephasing of electron spin qubits due to their interaction with nuclei in quantum dots. *Acta Phys. Pol. A* **119**, 576–587 (2011).
- Reilly, D. J. et al. Measurement of temporal correlations of the overhauser field in a double quantum dot. *Phys. Rev. Lett.* **101**, 236803 (2008).
- Malinowski, F. K. et al. Spectrum of the nuclear environment for GaAs spin qubits. *Phys. Rev. Lett.* **118**, 177702 (2017).
- Maździak, M. T. et al. Controllable freezing of the nuclear spin bath in a single-atom spin qubit. Preprint at <https://arxiv.org/abs/1907.11032> (2019).
- Freeman, B. M., Schoenfeld, J. S. & Jiang, H. Comparison of low frequency charge noise in identically patterned Si/SiO<sub>2</sub> and Si/SiGe quantum dots. *Appl. Phys. Lett.* **108**, 253108 (2016).
- Connors, E. J., Nelson, J., Qiao, H., Edge, L. F. & Nichol, J. M. Low-frequency charge noise in Si/SiGe quantum dots. *Phys. Rev. B* **100**, 165305 (2019).
- Petit, L. et al. Spin lifetime and charge noise in hot silicon quantum dot qubits. *Phys. Rev. Lett.* **121**, 076801 (2018).
- Mi, X., Kohler, S. & Petta, J. R. Landau–Zener interferometry of valley-orbit states in Si/SiGe double quantum dots. *Phys. Rev. B* **98**, 161404 (2018).
- Neumann, R. & Schreiber, L. R. Simulation of micro-magnet stray-field dynamics for spin qubit manipulation. *J. Appl. Phys.* **117**, 193903 (2015).
- Thorgrimsson, B. et al. Extending the coherence of a quantum dot hybrid qubit. *npj Quantum Inf.* **3**, 32 (2017).
- Andrews, R. W. et al. Quantifying error and leakage in an encoded Si/SiGe triple-dot qubit. *Nat. Nanotechnol.* **14**, 747 (2019).
- Cywiński, Ł., Lutchyn, R. M., Nave, C. P. & Das Sarma, S. How to enhance dephasing time in superconducting qubits. *Phys. Rev. B* **77**, 174509 (2008).

## ACKNOWLEDGEMENTS

The authors thank R. Huber and D. Weiss for technical support. This work has been funded by the German Research Foundation (DFG) within the project BO 3140/4-1 and under Germany's Excellence Strategy—Cluster of Excellence Matter and Light for Quantum Computing (ML4Q) EXC 2004/1—390534769. Project Si-QuBus received funding from the QuantERA ERA-NET Cofund in Quantum Technologies implemented within the European Union's Horizon 2020 Programme.

## AUTHOR CONTRIBUTIONS

L.R.S. and D.B. conceived the study. T.S. set up the experiment, performing the measurements and data analysis with A.H. and O.F., supported by L.R.S., A.S., F.S., and D.B. H.R. and N.V.A. fabricated the  $^{28}\text{Si}$  source material. F.S., A.S., and D.B. grew the heterostructure, fabricated the DQD device with support from K.S., and conducted the device simulation. L.R.S. and L.C. analyzed the contact hyperfine

interaction with support from T.S. and O.F. All authors discussed the results. D.B., L.R. S., T.S., F.S., O.F., A.H., A.S., and L.C. wrote the manuscript.

### COMPETING INTERESTS

The authors declare no competing interests.

### ADDITIONAL INFORMATION

**Correspondence** and requests for materials should be addressed to D.B. or L.R.S.

**Reprints and permission information** is available at <http://www.nature.com/reprints>

**Publisher's note** Springer Nature remains neutral with regard to jurisdictional claims in published maps and institutional affiliations.



**Open Access** This article is licensed under a Creative Commons Attribution 4.0 International License, which permits use, sharing, adaptation, distribution and reproduction in any medium or format, as long as you give appropriate credit to the original author(s) and the source, provide a link to the Creative Commons license, and indicate if changes were made. The images or other third party material in this article are included in the article's Creative Commons license, unless indicated otherwise in a credit line to the material. If material is not included in the article's Creative Commons license and your intended use is not permitted by statutory regulation or exceeds the permitted use, you will need to obtain permission directly from the copyright holder. To view a copy of this license, visit <http://creativecommons.org/licenses/by/4.0/>.

© The Author(s) 2020